


Reentrant melting and multiple occupancy crystals of bounded potentials: Simple theory and direct observation by molecular dynamics simulations

I. Nikiteas ^{*}

Applied Modelling and Computation Group, Department of Earth Science and Engineering, Imperial College London, Prince Consort Road, South Kensington, London SW7 2BP, United Kingdom

D. M. Heyes [†]

Department of Physics, Royal Holloway, University of London, Egham, Surrey TW20 0EX, United Kingdom



(Received 25 June 2020; accepted 10 September 2020; published 2 October 2020)

Aspects of the phase coexistence behavior of the generalized exponential model (GEM-m) and bounded versions of inverse power potentials based on theory and molecular dynamics (MD) simulation data are reported. The GEM-m potential is $\phi(r) = \exp(-r^m)$, where r is the pair separation and m is an adjustable exponent. A simple analytic formula for the fluid-solid envelope of the Gaussian core model which takes account of the known low- and high-density limiting forms is proposed and shown to represent the simulation data well. The bounded inverse power (BIP) potential is $\phi(r) = 1/(a^q + r^q)^{n/q}$, where a , n , and q are positive constants. The BIP potential multiple occupancy crystal or cluster crystals are predicted to form when $q > 2$ and $a > 0$, for $n > 3$, which compares with the corresponding GEM-m condition of $m > 2$. Reentrant melting should occur for the BIP potential when $q \leq 2$ and $a > 0$. MD simulations in which the system was gradually compressed at constant temperature using the BIP potential produced cluster states in the parameter domain expected but it was not possible to establish conclusively whether a multiply occupied crystal or a cluster fluid had formed owing to assembly structural fluctuations. The random phase approximation reproduces very well the BIP MD energy per particle without any discontinuities at the phase boundaries. The Lindemann melting rule is shown analytically to give a more rapidly decaying reentrant melting curve boundary than the so-called melting indicator (MI) empirical melting criterion which has also been investigated in this study. The MI model gives a better match to the high-density phase boundary for small m and q values.

DOI: [10.1103/PhysRevE.102.042102](https://doi.org/10.1103/PhysRevE.102.042102)

I. INTRODUCTION

Bounded pair (BP) potentials, which are those that are finite at the origin, have attracted much attention in recent decades as coarse-grained representations of polymer molecules in solution, and in various simulation models of liquids and soft matter [1–6]. They exhibit a number of novel phases not seen for typical interatomic potential systems. In the polymer case the Gaussian potential $\phi(r) = \epsilon \exp(-(r/\sigma)^2)$, where r is the pair separation, which is known as the Gaussian core model (GCM), has often been used [7,8]. In the present work the properties reported are expressed in units of the pair potential parameters, i.e., for length σ and for energy ϵ . In addition, the particle mass m is used for time-dependent properties. The temperature, T , is in units of ϵ/k_B , where k_B is Boltzmann's constant. The statistical mechanical properties and phase behavior of the GCM were determined about two decades earlier by Stillinger and co-workers (see, for example, Refs. [9–11]).

The GCM exhibits a solid phase for reduced temperatures below $T \simeq 0.009$ and has a lower and higher (“reentrant”) melting density at a given temperature, but is otherwise a fluid for all densities at higher temperatures. The fluid-solid coexisting density differences are very small on the scale of the diagram and the transition is weakly first order. This type of melting transition has been referred to as “cold melting” as it occurs at relatively large values of the coupling parameter (the ratio of the interaction potential at the mean nearest-neighbor separation to the thermal energy) which is two orders of magnitude larger than for typical liquids (e.g., the Lennard-Jones case). Cold melting occurs for the one component plasma, particularly when quantum effects are taken into account [12–14].

The phase diagram of the GCM system has subsequently been calculated more accurately using integral equation approaches [15,16], and directly by Monte Carlo simulation [17]. Recently the phase boundary of the exponential (EXP) potential [i.e., $\phi(r) = \exp(-r)$] has been determined by interface pinning and Clausius-Clapeyron equation tracking [18]. The phase behavior of the more general potential form,

$$\phi(r) = \exp(-r^m), \quad (1)$$

which is referred to as the generalized exponential model (GEM-m) [19], has also been investigated in the literature

^{*}ioannis.nikiteas17@imperial.ac.uk

[†]Author to whom correspondence should be addressed: david.hey@rhul.ac.uk

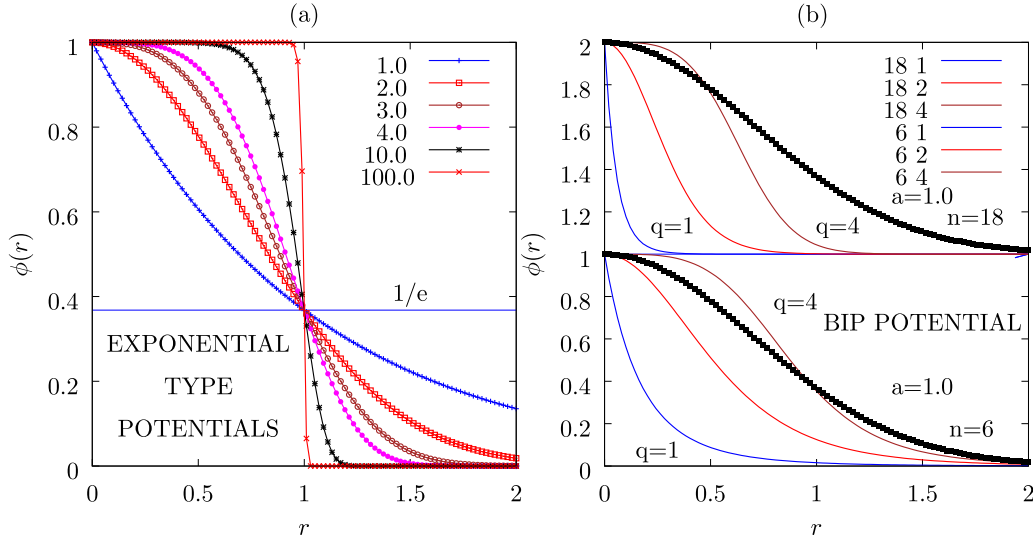


FIG. 1. (a) The general exponential potential (GEM- m) defined in Eq. (1) for several m values which are indicated in the figure. (b) The BIP potential given in Eq. (2). In the examples shown the bounding parameter, $a = 1$, and the values of n and q are given in that order in the figure. Data for $n = 18$ are given in the left-hand panel (shifted up by 1) and the $n = 6$ case is presented in the right-hand panel. The thick black lines on both frames are for the GCM potential which acts a typical reference bounded potential.

[20,21]. The GCM special case of the GEM class is of particular note as for $m \leq 2$ the crystal state has a second melting transition at high density (“reentrant melting”), whereas for $m > 2$ the system forms a multiple occupancy crystal (MOC) or cluster crystal in which more than one particle resides on each lattice site. This phenomenon is discussed further in Sec. II.

Another class of bounded interaction is an extension of the inverse power (IP) potential [22–25], which has an extra constant, a [26,27]. This bounded inverse power (BIP) potential has the analytic form

$$\phi(r) = \left(\frac{1}{a^q + r^q} \right)^{n/q}, \quad n > 3, \quad (2)$$

where q is a positive constant which can be noninteger, and a in Eq. (2) is taken to be positive in this work to allow for odd or noninteger values of q , and to ensure thermodynamic stability, $n > 3$ in three dimensions [28,29]. The potential is finite at the origin when $a > 0$, and $\phi(0) = a^{-n}$. The BIP potential in the $a \rightarrow 0$ limit tends to the IP potential [i.e., $\phi(r) = r^{-n}$], which has been widely used to represent small-molecule liquids and solids, and whose phase diagram was first determined comprehensively by Agrawal and Kofke [30,31]. The BIP potential could be used to represent the interaction between small molecular and polymer molecules in solution by adjusting the a parameter in Eq. (2), a regime in which the GCM might be considered to be too coarse grained. It was revealed in Ref. [32] that the BIP potential exhibits isomorphic scaling if a is made temperature, or equivalently density, dependent.

The phase diagrams of the BIP potential for different n , q , and a are not known, even approximately (apart from when $a = 0$). The purpose of this work is to determine some general features of the BIP phase diagrams using a combination of semiempirical models and more directly by molecular dynamics (MD) simulations. Comparisons with the GEM- m phase diagrams are made. The focus is mainly on real-space de-

scriptions of the phase behavior. The theoretical background, simulation details, and issues surrounding the phase diagram are presented in Sec. II. The simulation results and other computations are reported in Sec. III. A summary of the main conclusions is given in Sec. IV.

II. THEORY AND SIMULATION DETAILS

In this section the theory and techniques used to determine the phase diagrams of bounded potentials by approximate methods are discussed. The phase diagram is usually expressed in the form $T(\rho)$, where ρ is the number density of particles along the melting and freezing lines.

A. Generalized exponential model

Figure 1(a) shows the GEM- m class of pair potentials for different values of m . As the exponent increases, the potential approaches closer to the step or penetrable sphere potential [33] (i.e., $\phi(r) = \epsilon$, $r \leq \sigma$; $\phi(r) = 0$, $r > \sigma$, where $\epsilon > 0$). The hard-sphere potential is the $\epsilon \rightarrow \infty$ limit. The point-of-inflection distance, r_{pi} , which is also where the maximum repulsive force, f_{max} , occurs, is

$$r_{pi} = \left(1 - \frac{1}{m} \right)^{1/m}, \quad r_{pi} \rightarrow 1^- \text{ for } m \rightarrow \infty, \\ f_{max} = m r_{pi}^{m-1} \exp(-r_{pi}^m). \quad (3)$$

The phase diagram of the GCM or GEM-2 potential is considered first. The first part of the fluid-solid boundary at low density on the left-hand side reaches a maximum fluid-solid coexisting temperature, T_{max} , on increasing the density. At (very) low temperature an effective hard-sphere representation is accurate up to a temperature of about 0.0005 [15,16]. Above this temperature the hard-sphere model increasingly underestimates the coexistence density. With increasing density and temperature the density scaling exponent used in isomorph

theory [34] can be employed to trace out the next part of the melting line up to the maximum,

$$\gamma = \left(\frac{\partial \ln(T)}{\partial \ln(\rho)} \right)_{S^{\text{ex}}} = \frac{1}{3} \left(\frac{\partial \phi(r)}{\partial \ln(r)} \right)_{r=\bar{r}}, \quad (4)$$

where S^{ex} is the excess entropy and $\bar{r} \simeq \rho^{-1/3}$ leads to

$$T_f \simeq \exp(-\rho_f^{-2/3}/2). \quad (5)$$

The formula for T_f is obtained by integrating the expression in Eq. (4). The potential stiffness formula on the right-hand side of the first line of Eq. (5) is taken from Ref. [35]. The coexistence temperature given by the formula in Eq. (5) reaches a plateau at high density which is inconsistent with the known reentrant melting part of the phase diagram [15,16].

At higher densities in the reentrant region of the phase diagram an approximate analytic solution which represents the simulation data well is [36]

$$T_c(\rho) = A\rho \exp(-B\rho^{2/3}). \quad (6)$$

Note the difference in sign of the exponent of ρ of the two terms in ρ in Eqs. (5) and (6) which follows from the duality relations of the GCM of the low- and high-density boundaries at low temperature [10].

The fluid-solid boundary curve in the vicinity of the maximum in $T(\rho)$ is the most difficult region to represent analytically and needs a functional form which smoothly evolves between the low- and high-density limiting forms [i.e., Eqs. (5) and (6), respectively]. The low- and high-density limiting forms with different analytic density dependencies intersect at approximately the same density as the T_{max} value in the GCM literature from simulation. The intersection occurs, however, at $T_{\text{max}} \simeq 0.013$ rather than 0.009 from simulation.

There is a history of simple statistical theories of melting [37,38], which provide insights into the role played by the interaction potential and can be used to map out efficiently the phase diagram for a wide range of $\phi(r)$ parameters. For example, Lindemann's melting rule (LMR) [39] can be used to predict approximately the fluid-solid boundary envelope of the potential types employed in this study.

B. Lindemann's melting rule

Cell models of liquids and solids assume that the thermodynamic properties are determined by a representative atom interacting with its immediate neighbors [40,41]. Cell models of liquids were developed in the era before molecular simulation became available [42,43]. They were applied to hard-sphere systems in the 1960s and 1970s [44,45], and in the 2000s again to liquids [46] and for bounded potential systems [19]. LMR is a cell model for crystal melting which assumes that this occurs when the root-mean-square amplitude of the atom's thermal vibration in the crystal increases to a certain fraction of the nearest-neighbor distance, r_{nn} (about 10%), when the crystal is presumed to be unstable. No information about the coexisting fluid is required in LMR, and despite its simplicity, it has been used with some success in various fields [47–50]. The Lindemann parameter used in the theory is $\delta = \langle r^2 \rangle^{1/2}/r_{nn}$, where $\langle r^2 \rangle$ is the mean-square displacement of the atom from its average position. The potential energy of an atom in the crystal, Φ , leads to a confining force

constant, K , which within a simple harmonic approximation is

$$K \equiv m\Omega_E^2 = \frac{1}{3} \sum_i \nabla^2 \phi(r_i),$$

$$= \frac{1}{3} \sum_i \sum_\alpha \left(\frac{\phi'(r_i)}{r_i} \left[1 - \frac{\alpha_i^2}{r_i^2} \right] + \frac{\alpha_i^2}{r_i^2} \phi''(r_i) \right), \quad (7)$$

where $\phi' \equiv d\phi(r)/dr$ and $\phi'' \equiv d^2\phi(r)/dr^2$, and the summation is over all the lattice site vectors, i , omitting the zero displacement vector which is indicated by the prime on the summation. The summation is also over the three Cartesian coordinates, α , of the particles. The mass of the particle is m and Ω_E is the Einstein frequency [51]. We refer to the treatment considering, in principle, the whole lattice [i.e., Eq. (7)] as the harmonic lattice (HL) approximation or method.

In the Lindemann model the series in Eq. (7) is truncated at the first coordination shell, which means that the atom potential energy is approximated by $\Phi = N_{nn}\phi(r_{nn})$, where N_{nn} is the number of atoms at the nearest-neighbor distance, r_{nn} . The force constant in the Lindemann model, K_L , is therefore different from K . Then,

$$K_L = \frac{1}{3} N_{nn} \nabla^2 \phi(r)|_{r=r_{nn}},$$

$$= \frac{1}{3} N_{nn} \left(\frac{2}{r} \phi'(r) + \phi''(r) \right)_{r=r_{nn}},$$

$$= \frac{1}{3} \frac{N_{nn}}{r_{nn}^2} (2r\phi'(r) + r^2\phi''(r))_{r=r_{nn}},$$

$$= \frac{1}{3} \frac{N_{nn}}{r_{nn}^2} \frac{d}{dr} (r^2\phi'(r))_{r=r_{nn}}. \quad (8)$$

For harmonic motion, $k_B T = \langle r^2 \rangle K/3$, which, combined with the final expression in Eq. (8), substituting K_L for K , gives [48]

$$k_B T_m(\rho) = \frac{N_{nn}}{9} \delta^2 D,$$

$$D(r_{nn}) = \frac{d}{dr} [r^2 \phi'(r)]_{r=r_{nn}} = (2r\phi' + r^2\phi'')_{r=r_{nn}}. \quad (9)$$

For the generalized exponential potential, GEM-m, defined in Eq. (1) D is

$$D(r, m) = m^2 r^m (r^m - (1 + 1/m)) \exp(-r^m). \quad (10)$$

The condition, $D = 0$, is satisfied when $r = (1 + 1/m)^{1/m}$, and

$$r = ([3m + 1 \pm \sqrt{5m^2 + 2m + 1}]/2m)^{1/m}, \quad (11)$$

when $dD/dr = 0$. The nearest-neighbor distance is related to the number density through $r_{nn} = c/\rho^{1/3}$, where the constant c is

$$c = 1 \quad (\text{sc}),$$

$$c = 2^{1/6} = 1.122 \quad (\text{fcc}),$$

$$c = \frac{3^{1/2}}{4^{1/3}} = 1.091 \quad (\text{bcc}),$$

$$c = \left(\frac{6}{\pi} \right)^{1/3} = 1.241 \quad (\text{ws}), \quad (12)$$

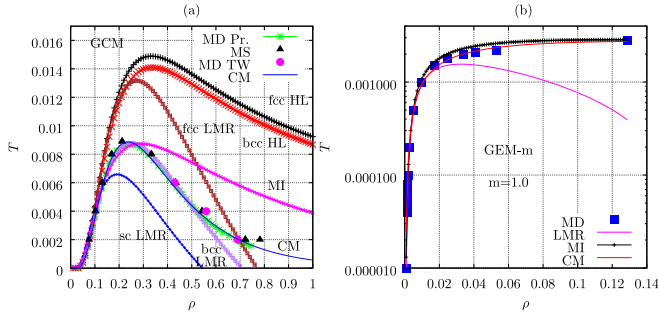


FIG. 2. (a) The fluid-solid phase diagram line of the GCM taken from Ref. [17] (“MD Pr.”), and Mausbach *et al.* [55] (“MS”). The green curve (MD Pr.) is the bcc/fcc boundary line from Ref. [17]. The system is a fluid at all temperatures above about 0.009. Direct phase change MD simulations from this work are denoted by “MD TW,” and “MI” is Eq. (15) with $L = 190$. (b) The phase diagram of the exponential potential. The magenta line is the LMR prediction. The solid blue squares are results from MD simulations [18]. The lines are the Lindemann (bcc) LMR formula and the melting indicator (MI) defined in Eq. (15) with $L = 190$. The fit formula in Eq. (14) denoted by “CM” is hardly distinguishable from the MI curve with these parameters.

for simple cubic (sc), face-centered cubic (fcc), body-centered cubic (bcc), and a Wigner-Seitz (ws) cell [52]. Khrapak and Saija [48] showed that the LMR reproduces many aspects of the phase diagram of the GCM, particularly in predicting the existence and value of T_{\max} and the upper part of the reentrant melting line. While there are extensions of the LMR in the literature which include, for example, a more realistic inherent frequency distribution [53] and a detailed exploration of the critical mean square displacement [49,54], the original LMR expression has the advantage that it produces simple mean field expressions for the melting envelope of bounded potentials which are analytically tractable.

The LMR expression [i.e., on taking the step from Eq. (7) to Eq. (8)] may not be a justifiable approximation in all circumstances, especially for long-range potentials (e.g., for m less than about 2 for GEM- m), when it truncates the interactions at a relatively short distance before the potential has decayed to an insignificant amount. The formula for T_m in the harmonic approximation is

$$k_B T_m(\rho) = \delta^2 r_{nm}^2 \frac{K}{3}, \quad (13)$$

where K is defined in Eq. (7). The summation is carried out over enough lattice vectors to give negligible error in K . Both the LMR and HL models for the melting line use the same Lindemann root-mean-square displacement criterion.

Figure 2(a) shows the predicted melting envelope for the GCM, using the LMR formula for the three crystalline forms referred to in Eq. (12). The height of the peak and width decreases through the sequence fcc, bcc, to sc, which is the same sequence of decreasing number of nearest neighbors. The greater N_{nn} the larger is the nearest-neighbor distance. The LMR fluid-solid boundaries are compared with the corresponding HL curves from Eq. (13). The LMR result for the bcc lattice using $\delta = 0.105$ gives very good agreement with the simulation data. The HL curves and the fcc LMR

curve are all above the simulation boundary line. The force constant increases when more interactions are included, while anharmonic contributions which are important at melting are neglected. This inconsistency might explain the reason why the low-coordination-number bcc LMR model coexistence curve agrees best with the simulation coexistence curve. The smaller number of neighbors of the bcc lattice reduces the force constant and thereby compensates for the absence of the softening effects of anharmonicity in the model.

C. Combined model (CM)

Figure 2(a) illustrates that the LMR model reproduces the low-density side and peak of the fluid-solid boundary of the GCM quite well but overestimates its rate of decay at very high density on the right-hand side of the solid-fluid coexistence envelope [48]. The exponential forms in Eqs. (5) and (6) can be combined in the following semiempirical formula:

$$T(\rho) = F \exp(-[G\rho^{-m/3} + H\rho^{m/3}]), \quad (14)$$

where F , G , and H are treated as parameters that can be fitted to numerical coexistence data. The formula in Eq. (14) is referred to here as the “combined model” (CM) as it satisfies the known density dependence of the GCM (or $m = 2$) in the low- and high-density limits. An m dependency has been introduced in the equation as an empirical generalization. The advantage of Eq. (14) is that it undergoes a smooth transition between the low-density and reentrant regimes. The highest melting temperature, T_{\max} , occurs at a density of ρ_{\max} . Equation (14) gives $\rho_{\max} = (G/H)^{3/2m}$, which substituted back into the equation returns T_{\max} . Figure 2(a) shows that the CM equation given in Eq. (14) fitted to the simulation data reproduces the whole GCM coexistence curve very well.

The LMR formula can be used to provide numerical data that can be fitted with Eq. (14) where simulation results are not available or give incomplete coverage of the phase diagram. Data for densities up to those on the reentrant side corresponding to $0.85T_{\max}$ were used for this fitting procedure. For the GCM case it was found that good agreement between Eq. (14) and the simulation data was obtained with LMR using $\delta = 0.105$ and taking the bcc lattice parameters with the LMR.

The $T_{\max}(m)$ and $\rho_{\max}(m)$ values obtained from LMR and CM fitted to second-order polynomials are presented in Table I for some values of m , and compared with the MD results. The polynomial fit parameters are given in Table II. Figure 3(a) presents the T_{\max} values as a function of m for the LMR calculations and CM fit formula. Figure 3(b) shows the corresponding ρ_{\max} m dependence using the fit formula parameters in Table II. For small m the maximum temperature part of the envelope is flatter and corresponding density more difficult to determine accurately, even by simulation [18]. The values of F , G , and H for each m are given in the Supplemental Material [56]. The figure also shows that the maximum temperature peaks from LMR and CM are hardly distinguishable for all the m values considered. For $m > 2$ the system exhibits a multiple occupancy crystal phase rather than reentrant melting and therefore some of the data in Fig. 3 represent metastable states. Nevertheless, these coexistence values are useful as they may indicate the highest temperatures at which a *single* occupancy crystal (SOC) (i.e., where

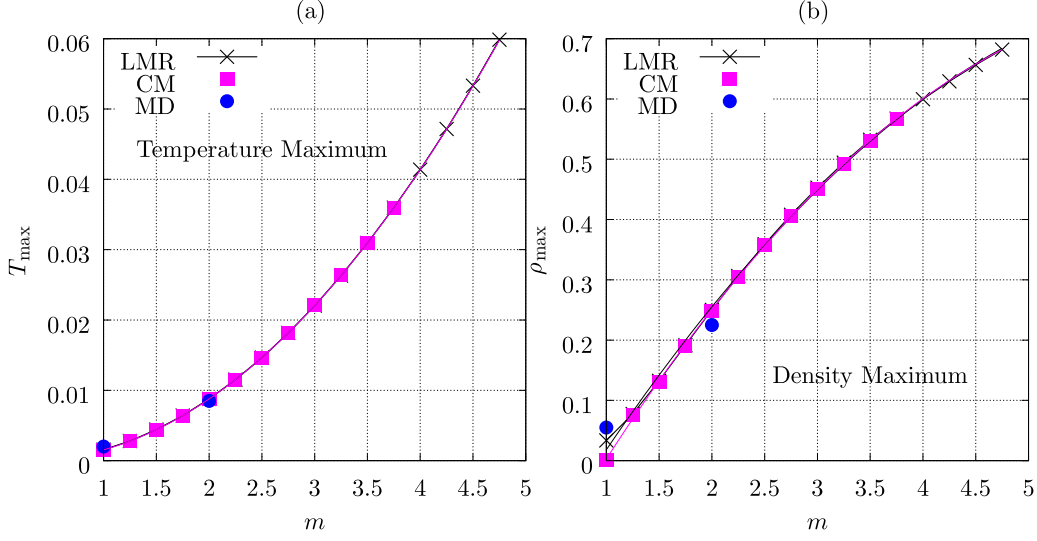


FIG. 3. (a) The dependence of T_{\max} on m for the GEM- m potential class. Data calculated numerically at intervals of 0.25 for m using the LMR and CM formulas. (b) The same as in (a) except that the dependence of ρ_{\max} on m is given. The polynomial fit parameters for this quantity are given in Table II.

there is only one atom per lattice site) would be stable and, through $\rho_{\max}(m)$, the width of the SOC solid part of the phase diagram.

D. Melting indicator

Another criterion for melting given in Ref. [48] was called the melting indicator (MI), which is similar to but a simpler formula than that of LMR. The definition is

$$k_B T = \frac{1}{L} (r^2 \phi''(r))_{r=\bar{r}}, \quad (15)$$

where $\bar{r} = 1/\rho^{-1/3}$ was used in Ref. [48], and L is an adjustable constant, ~ 200 . The advantage of MI is that it employs only the pair potential, and also only its second derivative. There is no dependence on a particular crystal form, unlike the LMR model.

TABLE I. The m dependence of the maximum temperature T_{\max} and the corresponding density ρ_{\max} along the T - ρ melting curve of the GEM- m potential system. The LMR method used Eq. (9) to produce values and then numerical evaluation and interpolation of the maximum. The CM method used Eq. (14) to fit the LMR data (up to $0.8T_{\max}$). See also Figs. 8(a) and 8(b). The raw data for these and other m values are given in the Supplemental Material [56].

m	ρ_{\max} LMR	T_{\max} LMR	ρ_{\max} CM	T_{\max} CM	ρ_{\max} MD	T_{\max} MD
1.0	0.033553	0.0015619	0.00102940	0.00155023	0.055	0.002 ^a
1.5	0.13244	0.0044155	0.130836	0.00440320		
2.0	0.25017	0.0087824	0.248101	0.00877042	0.225	0.0085 ^b
2.5	0.35908	0.014662	0.357202	0.0146580		0.015 ^c
3.0	0.45293	0.022055	0.451154	0.0220660		0.0245 ^c
3.5	0.53237	0.030962	0.530662	0.0309955		

^aData from Ref. [18].

^bData from Ref. [17].

^cData from this work.

For the GEM- m potential,

$$r^2 \phi'' = m^2 r^m (r^m - [1 - 1/m]) \exp(-r^m) \quad (16)$$

and $r^2 \phi'' = 0$ at $r = (1 - 1/m)^{1/m}$. From Eqs. (9) and (10) for LMR and Eq. (15) for MI, the corresponding densities are

$$\rho_{\text{LMR}}(T \rightarrow 0) = \frac{c^3}{(1 + 1/m)^{3/m}},$$

$$\rho_{\text{MI}}(T \rightarrow 0) = \frac{c^3}{(1 - 1/m)^{3/m}},$$

$$\frac{\rho_{\text{LMR}}(T \rightarrow 0)}{\rho_{\text{MI}}(T \rightarrow 0)} = \left(\frac{1 - 1/m}{1 + 1/m} \right)^{3/m} < 1, \quad (17)$$

and hence $\rho_{\text{LMR}}(T \rightarrow 0) < \rho_{\text{MI}}(T \rightarrow 0)$ for all m , which confirms that the LMR reentrant part of the fluid-solid coexistence line decays more rapidly than that of the MI formula for all m values. Figure 4(a) illustrates this behavior for two values of m . The maximum diminishes in height and extends to higher density as the potential becomes longer ranged (i.e., for smaller m). This feature makes MI more suitable than LMR for GEM- m potentials in the range $m < 2$ [18], which decay slowly on the high-density side of the fluid-solid boundary. The nearest-neighbor-only LMR model becomes increasingly

TABLE II. The formula coefficients for the maximum temperature of the solid phase, T_{\max} , and the density, ρ_{\max} , at which it occurs for the GEM- m potential as a function of m . The coefficients of the formula $X = a + bm + bm^2$, where X is either ρ_{\max} or T_{\max} for the CM formula given in Eq. (14) and LMR from Eq. (9), are shown.

X	Method	a	b	c
ρ_{\max}	LMR	-0.2621081	0.3017423	-0.02158801
T_{\max}	LMR	0.0003961835	-0.001861262	0.003026966
ρ_{\max}	CM	-0.2931339	0.3201196	-0.02417634
T_{\max}	CM	0.0003350350	-0.001812605	0.003017723

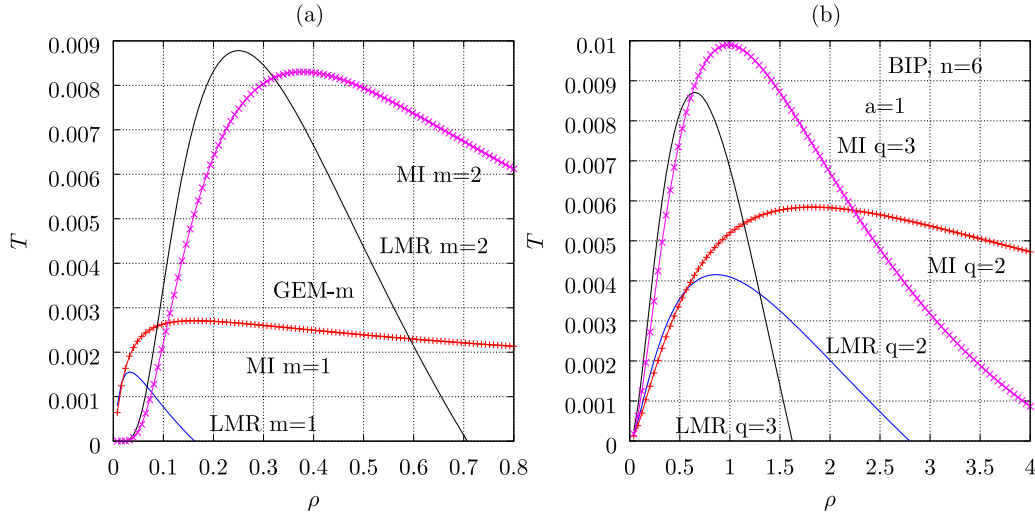


FIG. 4. (a) A comparison of the $T(\rho)$ fluid-solid boundary lines from Eqs. (9) and (10) for LMR and Eq. (15) for MI. The parameters used were for a bcc lattice with $L = 200$, for the GEM-m potential with $m = 1$ and $m = 2$. The figure confirms that the high-density boundary passes through $T = 0$ at a lower density for the LMR formula, as discussed in the main text in regard to Eq. (17). (b) The same as for (a) except using the curves for the BIP potential, i.e., where Eq. (21) is used in Eq. (9) (LMR) and Eq. (15) was taken for the MI method.

unrealistic in the small- m limit. Figure 2(b) shows that MI and CM expressions both fit well the coexistence envelope of the EXP (i.e., $m = 1$) simulation coexistence data of Bacher *et al.* [18].

The LMR has a maximum in $T(\rho)$ for all (nonzero) values of m . The maximum in LMR coincides with the maximum in D which occurs at the value of r given in Eq. (11). The maximum in $r^2\phi''$ which applies to MI occurs at

$$r = ([3m - 1 \pm \sqrt{5m^2 - 2m + 1}]/2m)^{1/m}, \quad (18)$$

which has a positive real value when $m \geq (1 + \sqrt{5})/5 = 0.6472$ (this result applies therefore for the exponential where $m = 1$). Therefore, to summarize, independent of m , the LMR fluid-solid boundary envelope range is narrower and decays more rapidly than the MI formula on the reentrant side of the fluid-solid phase boundary.

E. Molecular dynamics simulation

The paucity of molecular-simulation-derived coexistence data for the GEM-m potential (apart from $m = 1$ and 2) motivated the MD simulations reported here. The procedure adopted was to gradually increase the density of the system over a density range where it was anticipated the solid phase would exist, and to include the high-density reentrant melted or multiple occupancy crystal part of the phase diagram. The focus of the MD simulations was on the reentrant or multiple occupancy phase change, as the LMR is satisfactory for the low-density region freezing transition (i.e., to the left of the fluid-solid boundary maximum).

It is not easy to detect the phase boundary directly by simulation as, being weakly first order, typical order parameters such as the structure factor and potential energy changes are not strong and can therefore be ambiguous. The radial distribution function (RDF), $g(r)$ [57], was found to be the

most informative indicator of the structural changes taking place and possible phases.

The MD simulations were carried out at a fixed temperature. The modeled system contained typically 686–6750 particles in the MD cell, and the time step was $0.005/\sqrt{T}$. The simulations were commenced from a bcc or fcc lattice. For each temperature the density was increased by a small amount each time step so that the density range was covered in about 2×10^4 time steps. Then the density was reduced by the same number of steps back to the starting density. This process of increasing then decreasing the density back to the starting value, called a “cycle,” was carried out at least one time. Each cycle was started from a different set of particle velocities. The calculated quantities were stored in histograms as a function of density covering the whole density range, typically 50 bins for both increasing and decreasing parts of the cycle. Figure 2(a) shows that the reentrant melting point values obtained by this route for the GCM are in very good agreement with those in Ref. [17].

It is more problematic to simulate the phase diagram for potentials with small $m < 2$ as the temperature of the maximum in the solid-fluid coexistence boundary decreases with m . For example, for the exponential ($m = 1$) potential T_{\max} is about 0.004 [see Fig. 2(b)] as opposed to 0.009 for $m = 2$. The reentrant melting boundary is also rather flat with density for $m = 1$ and therefore very sensitive to temperature. This makes it difficult to choose state point parameters for the simulation that will pinpoint precisely the reentrant boundary line.

F. Bounded inverse power potentials

Figure 1(b) shows the BIP potential with $n = 6$ and 18 for $a = 1$. The BIP potentials for reasonable intermediate magnitude parameters are typically more rapidly decaying than their exponential counterparts shown in Fig. 1(a). The point

of inflection and maximum force values are

$$r_{pi} = a \left(\frac{(q-1)}{(n+1)} \right)^{1/q}, \quad f_{\max} = \frac{na^{q-1} \left(\frac{(q-1)}{(n+1)} \right)^{(q-1)/q}}{\left[a^q + a^q \left(\frac{(q-1)}{(n+1)} \right) \right]^{n/q+1}}. \quad (19)$$

The point of inflection tends to zero in the $q \rightarrow 1^+$ limit. The LMR quantity D in Eq. (9) is

$$D(r, n) = \left(\frac{nqr^{2q} \left(\frac{n}{q} + 1 \right)}{(a^q + r^q)^{n/q+2}} \right) - \left(\frac{n(q+1)r^q}{(a^q + r^q)^{n/q+1}} \right),$$

$$r^2 \phi'' = \left(\frac{nqr^{2q} \left(\frac{n}{q} + 1 \right)}{(a^q + r^q)^{n/q+2}} \right) - \left(\frac{n(q-1)r^q}{(a^q + r^q)^{n/q+1}} \right). \quad (20)$$

The value $r = a[(q+1)/(n-1)]^{1/q}$ satisfies the condition $D = 0$, and $r^2 \phi'' = 0$ when $r = a[(q-1)/(n+1)]^{1/q}$. As for GEM-m, a measure of the rate of decay of the fluid-solid boundary on the reentrant side for these two models can be made from the density in the zero-temperature limit, i.e.,

$$\rho_{\text{LMR}}(T \rightarrow 0) = c^3 a^{-3} \left(\frac{n-1}{q+1} \right)^{3/q},$$

$$\rho_{\text{MI}}(T \rightarrow 0) = c^3 a^{-3} \left(\frac{n+1}{q-1} \right)^{3/q},$$

$$\frac{\rho_{\text{LMR}}(T \rightarrow 0)}{\rho_{\text{MI}}(T \rightarrow 0)} = \left(\frac{(n-1)(q-1)}{(n+1)(q+1)} \right)^{3/q} < 1. \quad (21)$$

Equations (21) prove that the density in the $T \rightarrow 0$ limit is largest for the MI model for all positive values of n and q . The GEM-m potential exhibits the same relative order. Two examples of the LMR and MI coexistence envelopes are presented in Fig. 4(b). They show the same trends as the GEM-m potentials given in Fig. 4(a), in that they diminish in height and extend to higher density as the potential becomes longer ranged.

G. Multiple occupancy crystal criteria

Bounded potentials are separated into the class Q^+ , when the system exhibits an upper freezing temperature, T_{\max} , and reentrant melting, and systems of the so-called Q^\pm type, which freeze at all temperatures. The criteria for the different phases forming within a mean field approximation (MFA) are mainly based on a reciprocal-space-based analysis, [15–17, 58, 59]. Within the MFA, which is valid at high densities and/or high temperatures, it was shown that the MOC phase forms when the structure factor is negative for some regions of reciprocal space. The SOC-to-MOC transition density based on the MFA increases linearly with density. The key equations are

$$S(k) = \frac{1}{1 + \rho \tilde{\phi}(k)/T},$$

$$T = \frac{|\tilde{\phi}(k_*)| \rho}{1 - S_m^{-1}}, \quad S_m \cong 3,$$

$$T(\rho) = 1.5 |\tilde{\phi}(k_*)| \rho, \quad n_c = \frac{8\sqrt{2}\pi^3 \rho}{k_*^3}, \quad (22)$$

where $S(k)$ is the structure factor and $\tilde{\phi}(k_*)$ is the most negative value of the Fourier transform of the potential which occurs at the wave vector k_* . If the Fourier transform of the potential has negative regions the structure factor has many divergences indicating that the fluid is unstable within a mean field approximation. The Hansen-Verlet freezing criterion is that the first maximum in the structure factor is $S_m \simeq 3$. The k_* gives the lattice constant of the initial crystal which is independent of density thereafter according to the mean spherical approximation. For the GEM-m class of potential, $\tilde{\phi}(k)$ only has a negative region of $m > 2$. Analysis of the factors that determine repulsive bounded potential system clustering because of total potential energy barriers between the particles is given in Ref. [60].

The average number of particles on a lattice site, n_c , increases linearly with density according to the last formula in Eq. (22) [59]. The average number of particles associated with a lattice site, n_c , is

$$n_c = 1 + 4\pi \rho \int_0^{r_{nc}} r^2 g(r) dr, \quad (23)$$

where r_{nc} is the largest distance from the origin of the site used in its definition, a typical value being $r_{nc} \rho^{1/3} \simeq 0.35$, a practical definition used in analyzing the MD results here.

Likos *et al.* [21] proved that

$$6\pi^2 \phi''(r \rightarrow 0) = - \int_0^\infty k^4 \tilde{\phi}(k) dk, \quad (24)$$

and that in Eq. (24) if $\phi''(0) = 0$ then $\tilde{\phi}(k)$ must be negative for some region of k -space. This is the same requirement to form a MOC from a fluid within the MFA as given in Eq. (22). This criterion was applied in Ref. [61] to the GEM-m potential.

The condition $\phi''(0) = 0$ is satisfied for the BIP potential when $q > 2$ and $a > 0$, for all $n > 3$. Therefore, reentrant melting is predicted to occur using this criterion for the BIP potential when $q \leq 2$ and $a > 0$. This condition can be applied to other bounded potentials, for example, the algebraic hat (AH) potential, $\phi(r) = 1/(a + r^n)$, discussed in Ref. [27]. The second derivative of this potential in the $r \rightarrow 0$ limit is zero when $n > 2$ and $a > 0$ (i.e., the potential is bounded). The point of inflection occurs at $r = [an(n-1)/(n^2+1)]^{1/n}$. As a thermodynamic limit can only be defined for $n > 3$, then, using the $\phi''(0) = 0$ criterion, the MOC phase should appear rather than reentrant melting for all thermodynamically defined examples of this potential type. When $a = 0$ the IP potential is recovered, which exhibits neither reentrant melting nor a MOC phase.

While the phase behavior of cluster crystals at medium to high temperatures has been well examined, less is known about the phase diagram of the system at very low temperatures where the MFA is not accurate. Neuhaus and Likos [62] calculated the MOC behavior of the GEM-4 example in this low-temperature range up to high densities. They predicted a sequence of isostructural MOC transitions, a phenomenon that is returned to in Sec. III.

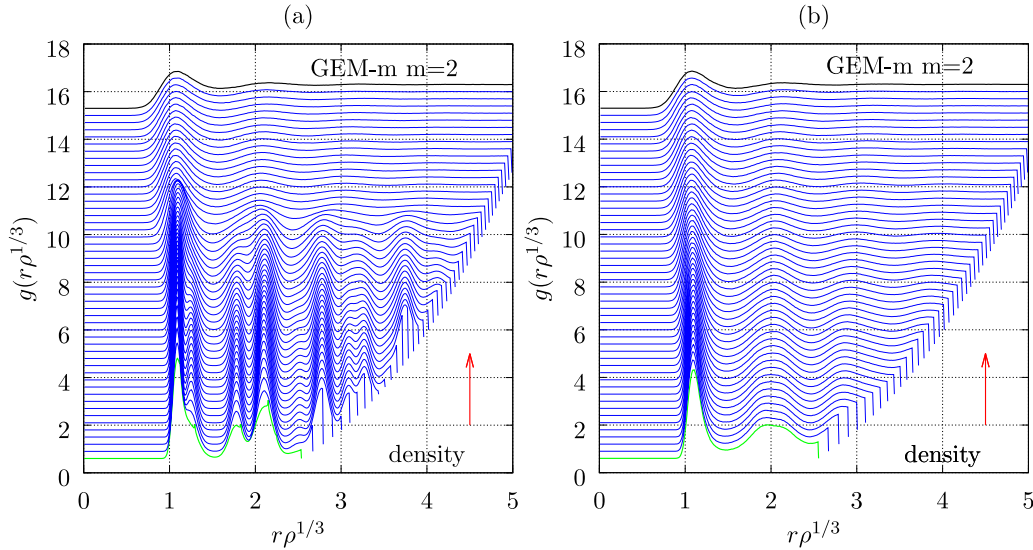


FIG. 5. The radial distribution functions of the exponential potential, $\exp(-r^m)$, where $m = 2$ (i.e., GCM) and $T = 0.002$. (a) The RDFs for densities increasing from bottom to top between $\rho = 0.12$ and 1.2 in 50 equal density intervals. The reentrant melting density is about 0.67 ± 0.02 . (b) The same as for (a) except the density is decreased in steps in reverse order. Again the lowest-density RDF is shown at the bottom. The system had 3456 particles and was started at low density from a bcc lattice.

III. RESULTS

This section concentrates on the MD simulation results and additional relevant theory.

A. MD for the GEM-m system

Figure 5(a) shows the RDF of the GCM at $T = 0.002$ which is very close to the baseline on a typical coexistence plot. The density is gradually increased with time starting from a bcc lattice structure. The lowest density is at the bottom of the figure, and the RDF of each increment of density is shown shifted upwards by a small constant amount to help discern the trends. The dimensionless (isomorph) quantity, $r\rho^{1/3}$, is used rather than the separation, r , because the peak positions in both crystal and fluid phases coincide better when density changes when plotted this way. This scaling accounts well for some of the “affine” consequences of the compression, and helps to identify any inherent structural or phase changes which will appear as departures from this scaling. The figure shows that the lattice structure disappears over a narrow density range for $\rho \simeq 0.67 \pm 0.02$ to an RDF typical of a fluid. This reentrant melting phase boundary is identified by the rapid disappearance of the solid peaks in the RDF on increasing the density. The quoted coexistence density was taken to be when the lattice structure started to decay noticeably, rather than when it had totally disappeared, to take into account any phase change delay owing to the finite (large) compression rate.

Figure 5(b) shows the corresponding set of RDF profiles to those in Fig. 5(a), but starting from the top of the figure, with the density gradually decreasing during the second half of each cycle. The fluid-to-solid transition after reentrant melting does not reappear, however, in Fig. 5(b); the liquid-like RDF peaks just progressively increase in height as the density decreases. Some indications of the impending crystal

are evident on the lowest few RDFs on the figure. The path followed in Fig. 5(a) causes the conditions where the lattice becomes unstable, whereas the path in Fig. 5(b) relies on the crystal nucleating which is, as confirmed in the figure, a much slower process which may not occur during the timescale of the expansion of the assembly in the simulation. The previous simulation was repeated starting from an fcc lattice structure with essentially the same reentrant melting density range. Further details are given in the Supplemental Material [56]. An alternative MD strategy was also explored, in which the temperature of the system was gradually increased at constant density. This type of simulation produced a melting transition in the density and temperature range predicted by the LMR model but typically overestimated the maximum melting temperature by about 5–10% for $m = 2$ and about 20% for $m = 3$. Homogeneous melting superheating is a well-known phenomenon in solids (e.g., it can be ~ 20 K for ice [63]). Again further details may be found in the Supplemental Material [56].

Figure 6 presents the same type of plot as in Fig. 5 in which the density is gradually increased and the temperature is kept constant, except that $m = 3$ and $T = 0.004$. This system, as expected, shows a transition at high density from a bcc starting lattice to a multiple occupancy phase (MOP), revealed by the peak in the RDF centered at $r = 0$. We were not able to definitively prove that the phase was a cluster fluid phase or MOC with large-amplitude fluctuations in the particle positions about their lattice sites. This transition appears at a density of 0.71 ± 0.02 in Fig. 6(a), and occurs in the present simulations over a relatively narrow density range when compared to the reentrant melting process seen in Fig. 5. A larger temperature dependence of the SOC-MOC coexistence boundary over a similar temperature range was predicted for the penetrable sphere potential [33], using a mixture of cell and density functional theory for the solid phase, with simulations for the fluid phase. Figure 6(b) shows

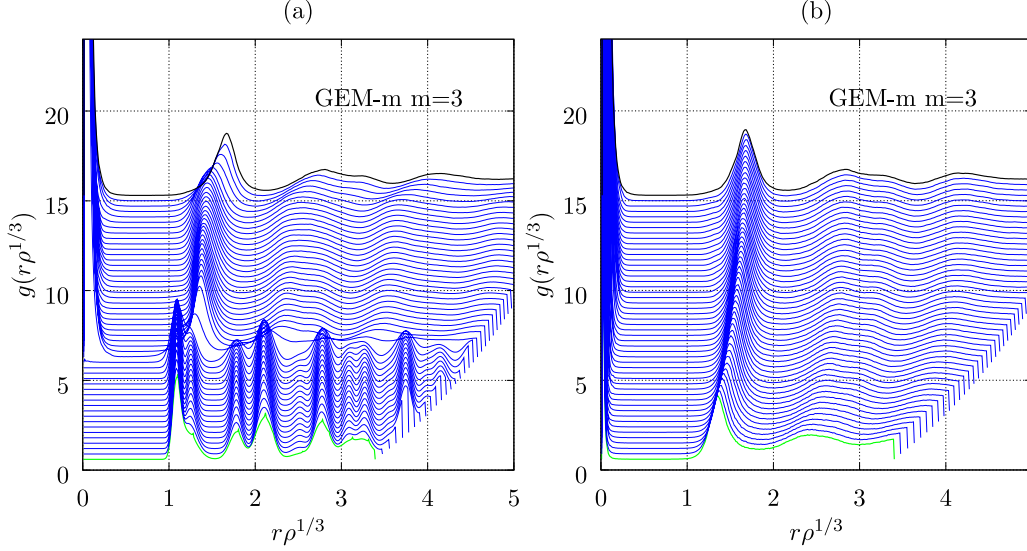


FIG. 6. As for Fig. 5 except that $m = 3$, and the starting lattice was a bcc crystal. The temperature is 0.004. The density range is between 0.05 and 1.2. The system transforms from a bcc crystal to a multiple occupancy state at a density of 0.71 ± 0.02 with $N = 3456$.

the RDFs at various densities during the decreasing density part of the cycle, which again reveals hysteresis and lag in reforming a SOC. The peak positions shift gradually with temperature, without sharp transitions, just as in Fig. 5(b).

Figure 7 shows the MOP transition densities obtained at different temperatures by MD superimposed on the phase diagram of the GEM-2.5 and GEM-3.0 systems in Figs. 7(a) and 7(b), respectively, as predicted by the LMR and CM formulas (see Fig. 2 also). Other simulations carried out for $2 < m < 3$ but not presented here reveal that the MOP transition occurs at a density typically in the range 0.65–0.75 which we found was relatively insensitive to temperature and m . This density, which is denoted by ρ_m , is much higher than the MFA MOC transition line [15,16,58]. This is not surprising as the MFA is

not valid in the low-density and -temperature part of the phase diagram. The temperature above which the fluid (or cluster fluid) was only evident in the simulations is indicated by a horizontal line in Figs. 7(a) and 7(b). They occur approximately near or slightly above the predicted T_{\max} from the LMR model.

Figure 6 which is for $m = 3$ starts the system from bcc crystal a density of 0.05 and temperature 0.004, which according to Fig. 7(b) is in the fluid region of the phase diagram. This is because, as may be observed when the density decreases starting from a fluid state, the crystallization process for the bounded potential systems is too slow to be observed in any routine MD simulation. As the high-density transition is of most interest here, it is appropriate to start the system off in the crystal form at the low-density state point even if that is in

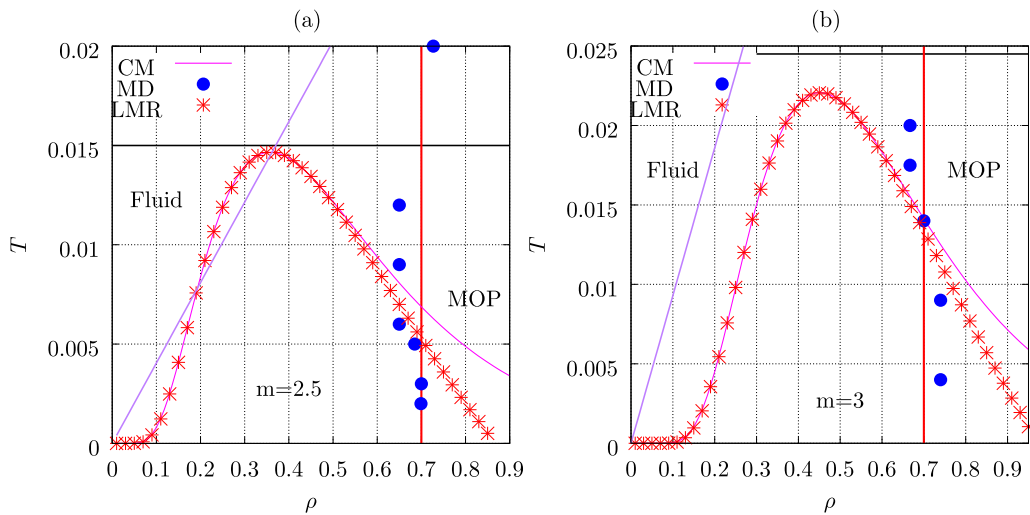


FIG. 7. The estimated phase diagrams for (a) $m = 2.5$ and (b) $m = 3.0$. The vertical red line and the solid blue circles indicate the MOP transition obtained from the simulations of this work. The sloping linear magenta line on the left-hand side of the figure denotes the fluid-solid MOC transition temperature from the MFA approximation from Eq. (22). For $m = 2.5$ and 3, $\phi(k_*)$ is -0.02908 and -0.06672 , respectively, employed in Eq. (22). The corresponding k_* are 5.60 and 5.33, respectively. The black horizontal line indicates the maximum in the fluid-solid envelope of this work obtained directly by MD.

the equilibrium fluid region. An fcc-to-bcc transition in the solid state is similarly unlikely to occur in any reasonable simulation time span, and that is why the bcc lattice was chosen to commence the simulation.

Simple models of the MOC transition were employed by Mladek *et al.* [64] which included a temperature dependence. In Ref. [61] models in the $T \rightarrow 0$ limit were solved. A similar combination of numerical and analytic treatments was carried out in this study (further details are presented in the Supplemental Material [56]). In the zero-temperature limit the Helmholtz free energy, F , tends to the interaction energy, U , which in the HL approximation is given by [64]

$$\frac{F(T \rightarrow 0)}{N} = \frac{U}{N} = u_0 = u_{01} + u_{02},$$

$$u_{01} = \frac{n_c - 1}{2} \phi(0), \quad u_{02} = \frac{n_c}{2} \sum_i \phi(r_i), \quad (25)$$

where N is the number of particles and all the particles are deemed to be on their regular lattice sites. The u_{01} term is for interactions between particles on the same lattice site, and u_{02} is for particles on different lattice sites. The summation is over a sufficient number of lattice vectors to give an adequately converged value of the potential energy. Note that it is the free energy per particle (not site) that is required to determine the stability of the system. Within the framework of the LMR nearest-neighbor cell approximation an analytically explicit expression for u_{02} is

$$u_{02} = \frac{n_c}{2} N_{nn} \exp\left(-\left[c\left(\frac{n_c}{\rho}\right)^{1/3}\right]^m\right). \quad (26)$$

An estimate of an upper bound of the SOC-MOC transition density can be made by solving Eqs. (25) and (26) analytically within this LMR nearest-neighbor framework approximation. This involves taking the first derivative of the potential energy with respect to n_c and setting it to zero to find the stationary point for n_c :

$$2u = (n_c - 1)\phi(0) + N_{nn}n_c\phi(r), \quad r = c\left(\frac{n_c}{\rho}\right)^{1/3}$$

$$\frac{d}{dn_c} 2u = 0 = \phi(0) + N_{nn}\left(1 - \frac{m}{3}r^m\right)\exp(-r^m),$$

$$\frac{1}{N_{nn}} = \left(\frac{m}{3}r^m - 1\right)\exp(-r^m), \quad (27)$$

taking $\phi(0) = 1$. For the right-hand side of the last expression in Eq. (27) to be positive and finite, then, $mr^m/3 > 1$ or $\rho < (m/3)^{3/m}c^3$ on taking $n_c = 1$. Above this density the SOC phase is predicted not to be stable. For the bcc unit cell and $m = 2$, $\rho_m \equiv \rho < 1/\sqrt{2} = 0.707$, which is in very good agreement with the values obtained by MD shown in Fig. 7. For the $m \rightarrow \infty$ (penetrable sphere) limit $\rho_m \rightarrow \sqrt{2}$ [58], which is the fcc close-packed limit of hard spheres (and for the bcc lattice, $\rho_m \rightarrow 3^{3/2}/4 = 1.30$) and is an upper bound.

For the BIP potential, the same treatment leads to

$$\frac{\phi(0)}{N_{nn}} = \frac{[(n/3) - 1]r^q - a^q}{(a^q + r^q)^{(n/q)+1}}. \quad (28)$$

As the top line on the left-hand side of Eq. (28) must be positive this requires that, for $n_c = 1$ and taking $\phi(0) = 1$

(i.e., $a = 1$),

$$\rho_m < \left(\frac{n}{3} - 1\right)^{3/q} c^3. \quad (29)$$

For the bcc lattice, $n = 12$ and $q = 2$, the SOC-MOC transition density $\rho_m < 27/4 = 6.75$, which is significantly higher than for any GEM-2 case. The softer the particle interaction (i.e., smaller n) the lower the threshold density into the MOC phase, while in the $n \rightarrow \infty$ (hard-sphere) limit the upper bound of the threshold tends to infinity.

To summarize, the $T \rightarrow 0$ analytic predictions of the multiple occupancy transition density agree well with those determined directly by MD in Fig. 7. For the GEM- m potential they predict a very slow increase in the value of ρ_m to its value in the penetrable sphere limit, which is the fcc close-packed limit of hard spheres. This is typically $m > 100$, depending on the details of the model. For the BIP systems ρ_m is predicted to be typically much higher.

B. MD for the BIP systems

It was shown in Sec. II that, using a MFA model, when $q \leq 2$ the BIP system should undergo reentrant melting but for $q > 2$ a MOC phase is predicted at high density. The BIP parameter q therefore to an extent takes the same role as m in the GEM- m potential.

Figure 8(a) shows the fluid-solid density-temperature melting curve for the inverse power potential (i.e., BIP with $a = 0$) obtained by the numerical integration of the Gibbs-Duhem equation (LMR) from Eqs. (9) and (10), also given in the figure, is seen to agree remarkably well with the literature melting curves. This suggests that LMR could also be a reasonable indicator of the corresponding BIP boundary lines, some examples of which are given in Fig. 8(b) for $q = 2$, $n = 6$, and variable a up to unity. One notable feature of Fig. 8(b) is the range in density of the BIP melting envelope compared to the GEM- m cases, using not too large or small potential parameters in both cases. For example, $\rho_m \simeq 2.3$ in the $T \rightarrow 0$ limit for the $a = 1$ case, which extends to much higher values when a is smaller (it will tend to ∞ when $a \rightarrow 0$).

Figure 9(a) presents further examples of the BIP melting curves, showing BIP coexistence curves calculated using the LMR method for $n = 6$ and $q = 4$ with variable a . Figure 9(b) explores the n dependence for $q = 2$ and $a = 1$. The high density range compared to the GEM- m curves in both frames again stands out. In both Figs. 9(a) and 9(b) the breadth and maximum range of ρ increase with n . Figures 8 and 9 also highlight the importance of the IP reference in determining significant aspects of the BIP phase diagrams for reasonable parameter ranges.

MD simulations were carried out using the BIP potential. Figure 10(a) shows the density dependence of the $q = 2$ RDF, starting from a bcc lattice with 3456 particles in the simulation cell. Density increases in equal increments between 0.5 and 20 from top to bottom in the figure were implemented. The system melted at $\rho \simeq 14.5$, as evidenced by the broadening and drop in height of the first peak, and the more gradual disappearance of the peaks at larger separation. This transition can be seen clearly in Fig. 10(b), which shows the height of

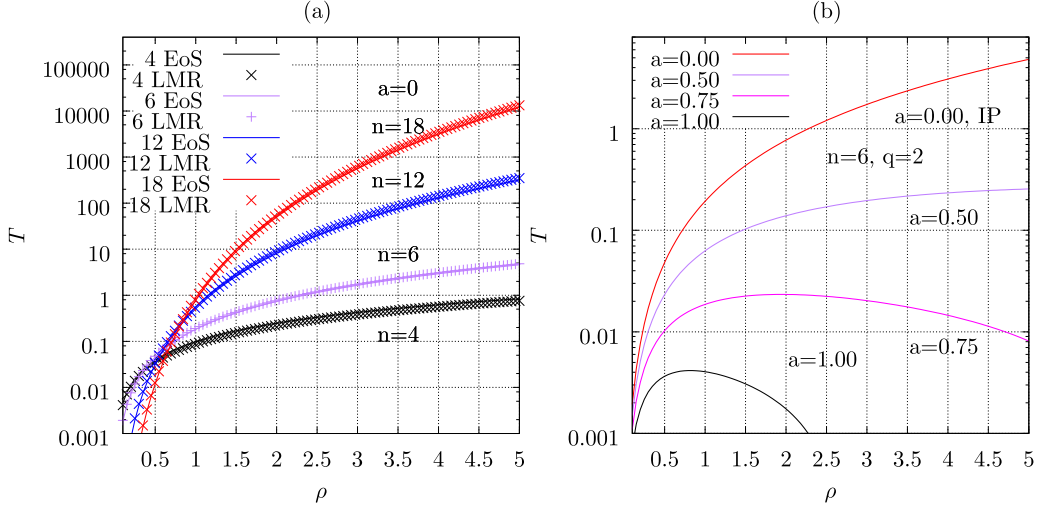


FIG. 8. (a) The density dependence of the fluid-solid coexistence temperature, T , of the inverse power [i.e., the BIP potential from Eq. (2) with $a = 0$]. The values of n are given in the figure. Continuous curves using IP scaling formulas benchmarked with Monte Carlo simulation data from Refs. [30,31] are shown. These are $T = \rho^{4/3}/10.2070$, $T = \rho^{6/3}/5.4636$, $T = \rho^{12/3}/1.9659$, and $T = \rho^{18/3}/1.2929$ for $n = 4, 6, 12$, and 18 , respectively. Also given as symbols are the values from the Lindemann formulas (LMR) in Eqs. (9) and (10). The bcc lattice formula gave the best agreement with the simulation-derived equation of state data (EoS) using LMR on taking $r_{nn} = (\alpha^{3/2}/4\rho)^{1/3}$ where the factor $\alpha = 0.95$ to improve agreement with the EoS. (b) The same as for (a) except the corresponding BIP potential curves are presented adopting variable a (given in the figure) using $n = 6$ and $q = 2$ in each case.

the first peak in $g(r)$ as a function of density. There is a sharp decrease in this value at $\rho \simeq 14.5$, which indicates the transition from SOC crystalline order to a fluid state (i.e., reentrant melting). Figure 10(b) shows the density dependence of the ratio of the value of the first minimum divided by the first maximum in $g(r)$. The ratio starts to increase from zero in the transitional density range associated with melting, as is to be expected. Figure 10(b) also shows the density dependence of the potential energy per particle, u , which increases linearly with density over the majority of the density range without showing any discontinuity or noticeable change of slope throughout the melting transition. This line is predicted

well using the random phase approximation (RPA) [36,65],

$$u = \frac{1}{2}(\tilde{\phi}(0)\rho - 1). \quad (30)$$

For the BIP potential with $n = 12$ and $q = 2$, then $\tilde{\phi}(0) = \pi^2 105/[1920a^9]$ [26], where $a = 1$ in the MD simulations. This is shown as the blue line in Fig. 10, which is seen to agree very well with the MD data. The very small difference between the potential energy of the fluid and SOC at coexistence for the GCM was discussed within the RPA framework in Ref. [36].

Figure 11 is as Fig. 10, except $q = 2.1$. Figure 11(a) shows that the initial bcc crystalline state first melts into a (single

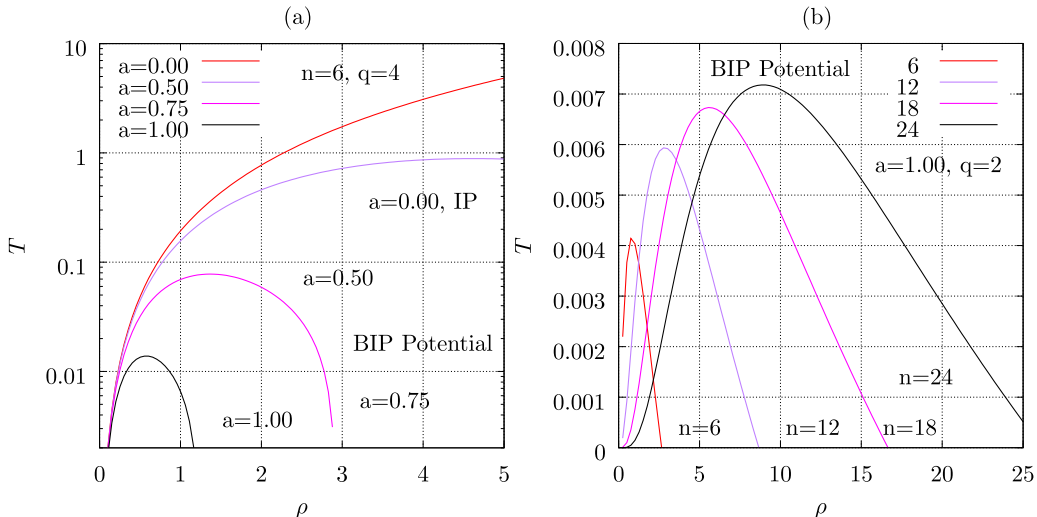


FIG. 9. As for Fig. 8 except (a) the LMR coexistence curve for the BIP potential systems with $n = 6$ and $q = 4$ with variable a are shown. (b) The same as for (a) except $q = 2$, $a = 1$, and the indicated BIP exponent, n , is varied.

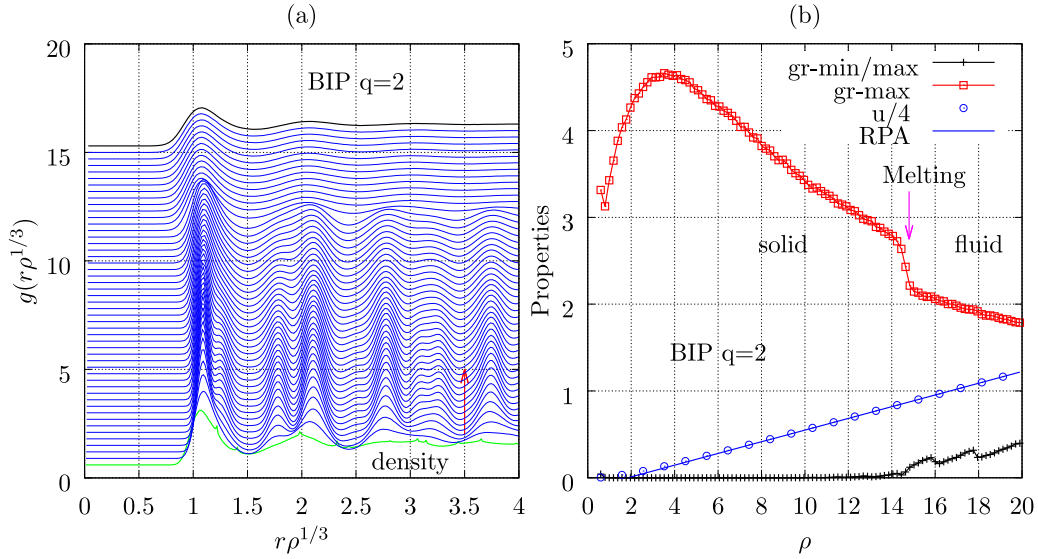


FIG. 10. (a) Radial distribution functions plotted as a function of $r\rho^{1/3}$ for the BIP potential in the density range 0.5–20.0. Density increases from bottom to top in the figure. The simulations started from a bcc lattice and $N = 3456$. The parameters used were $a = 1$, $n = 12$, and $q = 2$. (b) The variation in the values of certain properties as a function of density during the increasing density part of the MD cycle for the simulation of (a). The height of the first peak in $g(r)$, or “gr-max,” is shown. The ratio of the first RDF minimum to the first maximum, or “gr-min/max,” is also given. The average potential energy per particle, u , is presented as open circles. The solid blue line coincident with the u data is from the RPA formula in Eq. (30), where $\tilde{\phi}(0) = 0.539744$.

occupancy) fluid state. At higher density the system develops a peak at $r = 0$ in the RDF indicative of a MOP state, which could be a cluster fluid. These transitions are reflected in the density variation of certain system properties which are presented in Fig. 11(b). The reentrant melting phase occurs at $\rho \simeq 11$ and the fluid-MOP phase transition at $\rho \simeq 21$. The MOP phase is distinguished by the appearance of a peak centered at $r = 0$ and $n_c > 1$. The ratio, $g(r_{\min})/g(r_{\max})$, is only significantly above zero in the intermediate fluid region. The potential energy per particle increases linearly with density,

even during the two phase transitions, and shows excellent agreement with the RPA analytic formula.

Figure 12 is as for Fig. 11 but with $q = 2.2$. In this case the SOC-to-MOP transition is sharp (without any intervening fluid phase). The system undergoes a series of well-defined MOP-to-MOP transitions in which the density-scaled nearest-neighbor distance, r_{\max} , is constant over a certain density range and then suddenly increases to a new value in well-defined density increments, which coincide with increases in n_c . The number density of lattice sites decreases as the

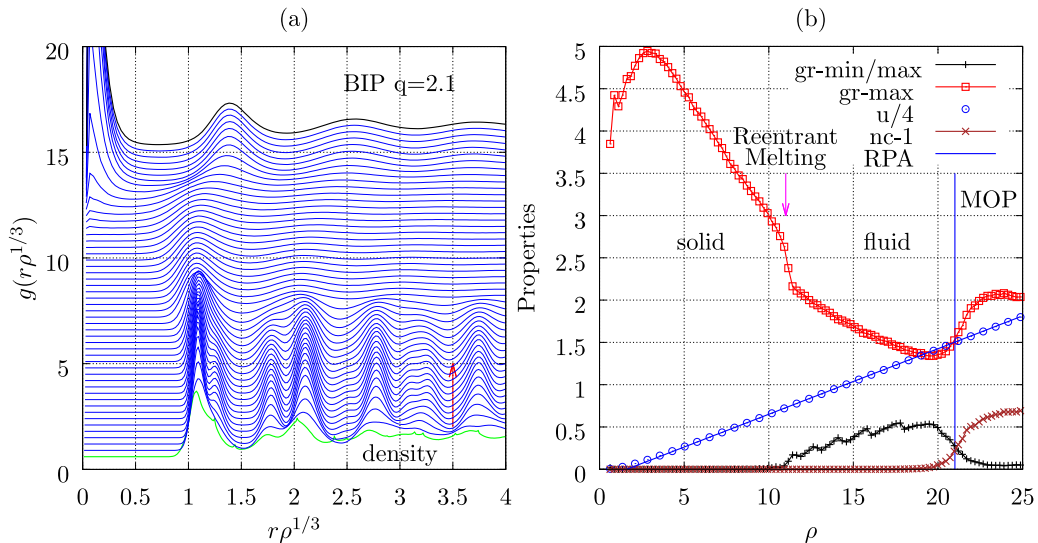


FIG. 11. As for Fig. 10, except $q = 2.1$ and $\tilde{\phi}(0) = 0.620338$ which was obtained by numerical integration. The other parameters used were $T = 0.002$, $N = 3456$, $a = 1$, and $n = 12$. (b) The average occupancy number, n_c , is also presented as $n_c - 1$. The particle number density range covered was from 0.5 to 25.

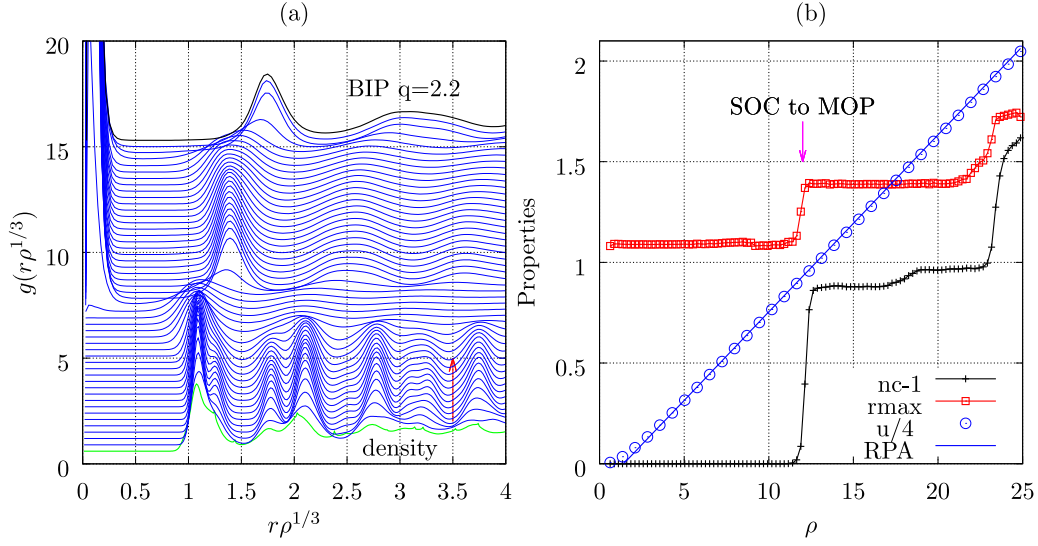


FIG. 12. As for Fig. 11, except $q = 2.2$ and the position of the first peak in $g(r)$, or “rmax,” is shown in (b). The parameters used were $T = 0.002$, $N = 3456$, $a = 1$, and $n = 12$. The density range is from 0.5 to 50. The RPA constant for Eq. (30) is $\tilde{\phi}(0) = 0.703419$.

occupancy of each site increases subject to the constraint that $N = n_c N_c$, where N_c is the number of sites in the simulation cell. This stepwise evolution of the MOP phase with increasing density was observed by MD for all N up to 6750 (the highest number considered), an example of which with $q = 2.3$ is given in Fig. 13.

The evidence from simulations with different N is that the sequence of “steps” in n_c observed in the present simulations is not a finite system size and periodic boundary effect. As mentioned in Sec. II this behavior was predicted by Neuhaus and Likos [62], whose modeling work on GEM-4 revealed a series of MOC crystals with increasing lattice site occupancies, appearing in steps separated by coexistence states populated by lattices with different n_c . In the present simulations (e.g., Fig. 13) the steps are manifest in

density ranges where the first peak in the RDF occurs at a constant $r\rho^{1/3}$ value. These steps are separated by small transitional density ranges in which the peak position changes significantly.

Figure 14 shows two examples of the particle assembly at an instant in the simulation. Representative examples for the GEM-4 and BIP systems are shown in Figs. 14(a) and 14(b), respectively. For GEM-4, $T = 0.4$ and $\rho = 7.0$, and for the BIP example, $T = 0.002$, $n = 12$, $q = 2.20$, and $a = 1.0$. In both cases there is evidence of separation of the particles into small clusters, which is also evident in the RDFs of Figs. 6 for GEM and in Figs. 11–13 for BIP. At any instant there is a distribution of cluster sizes, including monomers. The clusters are smaller in the BIP case, as this state is closer to the reentrant transition than the GEM example.

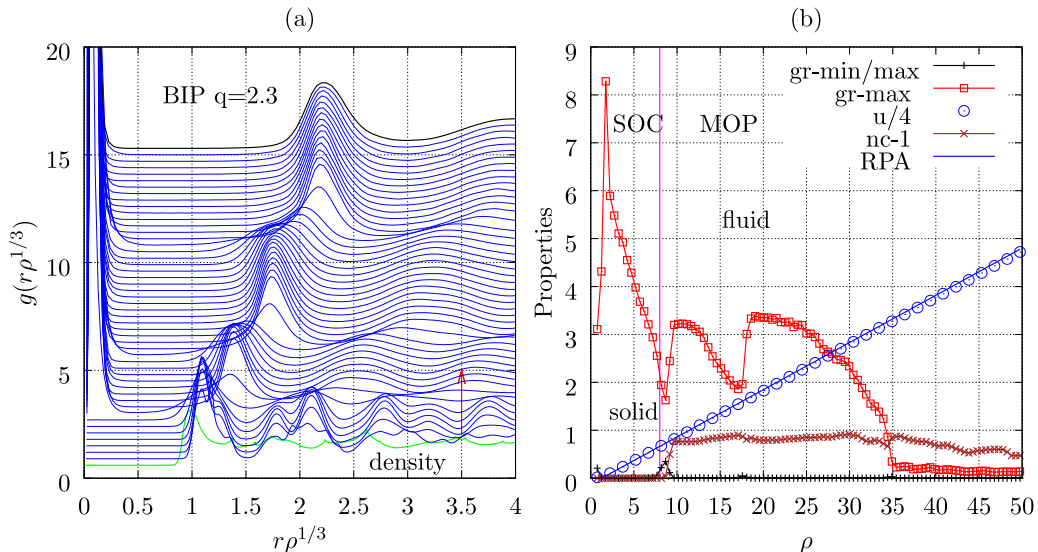


FIG. 13. As for Fig. 12, except $q = 2.3$ and the position of the first peak in $g(r)$, or “rmax,” is shown in (b). The density range is from 0.5 to 50, and the other parameters are $N = 6750$, $T = 0.002$, $a = 1$, and $n = 12$. The RPA constant for Eq. (30) is $\tilde{\phi}(0) = 0.788368$.

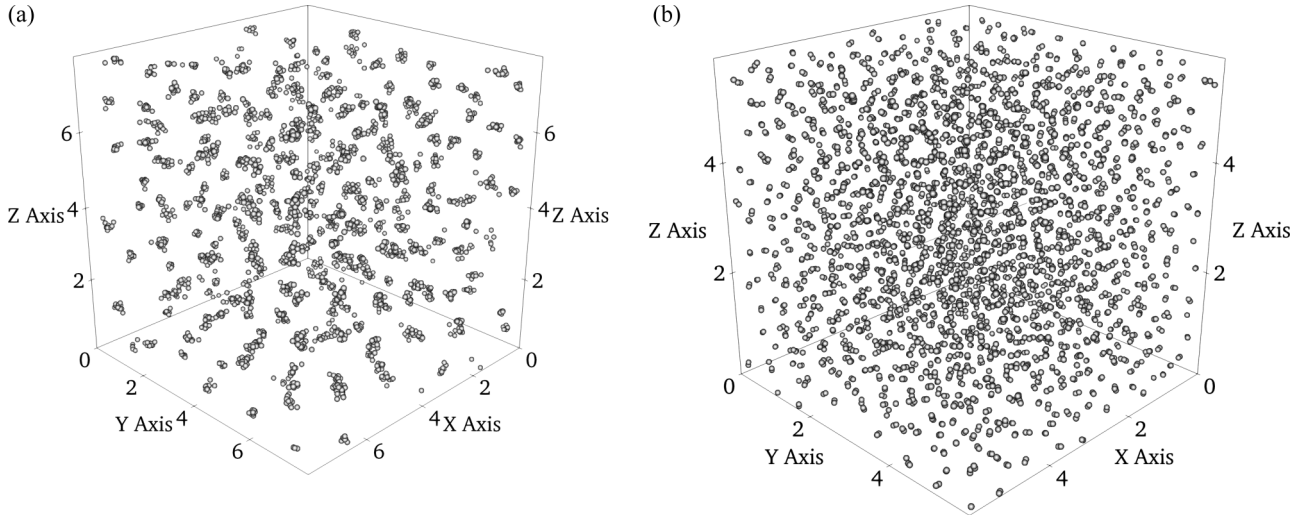


FIG. 14. Perspective snapshot particle assembly images showing clustering. (a) GEM with $T = 0.4$, $\rho = 7.0$, $m = 4.0$, and $N = 3456$. (b) BIP with $T = 0.002$, $n = 12$, $q = 2.20$, $a = 1.0$, and $N = 3456$.

IV. CONCLUSIONS

Some aspects of the high-density transition from a single occupancy crystal (SOC) to a (reentrant) fluid or multiple occupancy state for bounded potentials are revealed using molecular dynamics (MD) simulations. The MD simulations generated these transitions directly by gradual isothermal compression of the assembly of particles. This is an investigation for the phase diagram of the bounded inverse power (BIP) potential.

The Lindemann melting model (LMR), which provides a criterion for melting in terms of the first two derivatives of the pair potential at the nearest-neighbor distance in a lattice is shown to reproduce well the high-density instability of the single occupancy crystal. This approach proved most accurate for the generalized exponential potential (GEM-m) for about $m \geq 2$, whereas the so-called melting indicator formula, which does not rely on an assumed lattice form, proved progressively more realistic with decreasing m below 2. The high-density solid phase becomes broader in density and flat at the top (exemplified by the $m = 1$ or EXP potential).

The MD and LMR coexistence data (over a limited range) were used to parametrize a simple formula for the Gaussian core model ($m = 2$) phase boundary envelope, given in Eq. (14), which reproduces well the exact low- and high-density dependencies. The formula was generalized to apply to a wider range of m for the GEM-m class of potential, and also for the BIP potential systems.

It is shown analytically using the $\phi''(0) = 0$ single-to-multiple-occupancy crystal transition criterion derived by Likos *et al.* [21] and directly by MD simulation that the bounded inverse power (BIP) potential system can also form a multiple occupancy phase providing the q parameter is greater than 2 (independent of n and $a > 0$), which is similar to the $m > 2$ criterion for the GEM potential. For large m and q values greater than 2 the potential becomes flatter near the origin and the system behavior starts to follow that of the penetrable sphere (PS). As for the GEM-m potential, although an assembly of clusters was evident for m and q above 2, evidence of

the MOC crystalline state itself based on a large number of simulations at different state points was not conclusive.

The BIP systems with not too extreme parameter values have fluid-solid boundary envelopes which extend to much higher densities than those formed of the GEM-m potentials (e.g., ~ 10 or higher for relatively modest values of a , n , and q). The BIP potentials decay more rapidly at intermediate separation than otherwise-similar-in-appearance exponential-type examples. They retain some characteristics of the inverse power reference which does not exhibit reentrant melting or MOC formation.

It is shown that the random phase approximation is remarkably good in reproducing the potential energy per particle from the BIP MD simulations, even in the solid phase, as is revealed in Figs. 10–13. There is no noticeable discontinuity or change of slope at the fluid-solid phase boundaries. This behavior was noted in Ref. [36] for the GCM and it is demonstrated that the BIP potential follows the same trend (at least for $a = 1$, $q = 2$, and $n = 12$ states specifically examined).

The LMR model is shown to reproduce very well the fluid-solid freezing line of the inverse power fluid (i.e., $a = 0$), and it is used to predict the melting envelope of the BIP potential system. It is proved analytically that the LMR expression for the fluid-solid coexisting boundary envelope always decays more rapidly on the reentrant side than that predicted by MI for both generalized exponential (GEM-m) and BIP potential systems. The MI is a more accurate model for long-ranged potentials but can underestimate the rate of decay for more rapidly decaying potentials (e.g., $m > 2$ in the GEM-m cases).

A rigorous numerical evaluation of the phase diagrams of these systems by simulation is a formidable task because of the large BIP parameter space and the weakness of the transitions which cause hysteresis issues for melting and crystallization. In this work selected simulations have been carried out to illustrate in a more direct way the key features of the phase diagram of these potentials. A more systematic characterization of the phase diagram probably requires a better targeted method such as that employed in Ref. [17] for the GCM potential.

ACKNOWLEDGMENTS

D.M.H. would like to thank Dr. T. Crane (Department of Physics, Royal Holloway, University of London, UK) for helpful software support.

-
- [1] J. M. V. A. Koelman, P. J. Hoogerbrugge, P. Español, and P. Warren, *Europhys. Lett.* **19**, 155 (1992).
 - [2] K. E. Novik and P. V. Coveney, *J. Chem. Phys.* **109**, 7667 (1998).
 - [3] J. Monaghan, *Annu. Rev. Fluid Mech.* **44**, 323 (2012).
 - [4] W. G. Hoover and H. A. Posch, *Phys. Rev. E* **54**, 5142 (1996).
 - [5] P. Español and M. Revenga, *Phys. Rev. E* **67**, 026705 (2003).
 - [6] P. M. Kulkarni, C.-C. Fu, M. S. Shell, and L. Gary Leal, *J. Chem. Phys.* **138**, 234105 (2013).
 - [7] A. A. Louis, P. G. Bolhuis, R. Finken, V. Krakoviack, E. J. Meijer, and J. P. Hansen, *Physica A*, **306**, 251 (2002).
 - [8] J. P. Hansen, C. I. Addison, and A. A. Louis, *J. Phys.: Condens. Matter* **17**, S3185 (2005).
 - [9] F. H. Stillinger, *J. Chem. Phys.* **65**, 3968 (1976).
 - [10] F. H. Stillinger, *Phys. Rev. B* **20**, 299 (1979).
 - [11] F. H. Stillinger and D. K. Stillinger, *Physica A* **244**, 358 (1997).
 - [12] C. N. Likos and N. W. Ashcroft, *Phys. Rev. Lett.* **69**, 316 (1992).
 - [13] M. D. Jones and D. M. Ceperley, *Phys. Rev. Lett.* **76**, 4572 (1996).
 - [14] S. M. Stishov, *J. Exp. Theor. Phys. Lett.* **67**, 90 (1998).
 - [15] C. N. Likos, *Phys. Rep.* **348**, 267 (2001).
 - [16] C. N. Likos, *Soft Matter* **2**, 478 (2006).
 - [17] S. Prestipino, F. Saija, and P. V. Giaquinta, *Phys. Rev. E* **71**, 050102(R) (2005).
 - [18] U. R. Pedersen, A. K. Bacher, T. B. Schröder, and J. C. Dyre, *J. Chem. Phys.* **150**, 174501 (2019).
 - [19] B. M. Mladek, P. Charbonneau, C. N. Likos, D. Frenkel, and G. Kahl, *J. Phys.: Condens. Matter* **20**, 494245 (2008).
 - [20] B. M. Mladek, M. Feraud, G. Kahl, and M. Neumann, *Condens. Matter Phys.* **8**, 135 (2005).
 - [21] C. N. Likos, B. M. Mladek, D. Gottwald, and G. Kahl, *J. Chem. Phys.* **126**, 224502 (2007).
 - [22] J. P. Hansen and I. R. McDonald, *Theory of Simple Liquids: With Applications to Soft Matter: Fourth Edition* (Elsevier/AP, Amsterdam, 2013).
 - [23] N. H. March and M. P. Tosi, *Introduction to Liquid State Physics* (World Scientific, Singapore, 2002).
 - [24] W. G. Hoover, D. A. Young, and R. Grover, *J. Chem. Phys.* **56**, 2207 (1972).
 - [25] J.-P. Hansen and D. Schiff, *Mol. Phys.* **25**, 1281 (1973).
 - [26] G. Rickayzen and D. M. Heyes, *Mol. Phys.* **109**, 1373 (2011).
 - [27] D. M. Heyes, *Chem. Phys.* **513**, 174 (2018).
 - [28] M. E. Fisher and D. Ruelle, *J. Math. Phys.* **7**, 260 (1966).
 - [29] D. M. Heyes and G. Rickayzen, *J. Phys.: Condens. Matter* **19**, 416101 (2007).
 - [30] R. Agrawal and D. A. Kofke, *Phys. Rev. Lett.* **74**, 122 (1995).
 - [31] R. Agrawal and D. A. Kofke, *Mol. Phys.* **85**, 23 (1995).
 - [32] I. Nikiteas and D. M. Heyes, *J. Chem. Phys.* **150**, 144504 (2019).
 - [33] C. N. Likos, M. Watzlawek, and H. Löwen, *Phys. Rev. E* **58**, 3135 (1998).
 - [34] J. C. Dyre, *J. Phys. Chem. B* **118**, 10007 (2014).
 - [35] S. A. Khrapak and G. E. Morfill, *Phys. Rev. Lett.* **103**, 255003 (2009).
 - [36] A. Ikeda and K. Miyazaki, *J. Chem. Phys.* **135**, 024901 (2011).
 - [37] W. G. Hoover and M. Ross, *Contemp. Phys.* **12**, 339 (1971).
 - [38] Y. Rosenfeld, *Mol. Phys.* **32**, 963 (1976).
 - [39] F. A. Lindemann, *Phys. Z.* **11**, 609 (1910).
 - [40] J. E. Magee and N. B. Wilding, *Mol. Phys.* **100**, 1641 (2002).
 - [41] B. L. Holian, *Phys. Rev. B* **22**, 1394 (1980).
 - [42] J. A. Barker and E. A. Guggenheim, *Proc. R. Soc. London Ser. A* **230**, 390 (1955).
 - [43] J. A. Barker, *Lattice Theories of the Liquid State*, International Encyclopedia of Physical Chemistry and Chemical Physics, Topic 10: The Fluid State Vol. 1 (Pergamon, Oxford, 1963).
 - [44] W. G. Hoover and F. H. Ree, *J. Chem. Phys.* **47**, 4873 (1967).
 - [45] W. G. Hoover, W. T. Ashurst, and R. Grover, *J. Chem. Phys.* **57**, 1259 (1972).
 - [46] R. H. Henchman, *J. Chem. Phys.* **126**, 064504 (2007).
 - [47] G. Rastelli and E. Cappelluti, *Phys. Rev. B* **84**, 184305 (2011).
 - [48] S. A. Khrapak and F. Saija, *Mol. Phys.* **109**, 2417 (2011).
 - [49] S. N. Luo, A. Strachan, and D. C. Swift, *J. Chem. Phys.* **122**, 194709 (2005).
 - [50] M. Ross, *Phys. Rev.* **184**, 233 (1969).
 - [51] U. Balucani and M. Zoppi, *Dynamics of the Liquid State*, Oxford Series on Neutron Scattering in Condensed Matter (Clarendon Press, Oxford, 1995), p. 18.
 - [52] F. E. Leys, N. H. March, and M. L. Zhang, *Phys. Chem. Liq.* **42**, 217 (2004).
 - [53] F. Mulargia, F. Quarenzi, and E. Boschi, *Nuovo Cimento C* **10**, 479 (1987).
 - [54] C. Chakravarty, P. G. Debenedetti, and F. H. Stillinger, *J. Chem. Phys.* **126**, 204508 (2007).
 - [55] P. Mausbach, A. Ahmed, and R. J. Sadus, *J. Chem. Phys.* **131**, 184507 (2009).
 - [56] See Supplemental Material at <http://link.aps.org/supplemental/10.1103/PhysRevE.102.042102> for the values of F , G , and H of Eq. (14) for each value of m . Some additional radial distribution function figures and property variations with density at constant temperature and with temperature at constant density are presented. Several static lattice model predictions of the SOC-to-MOC transition are compared with other semiempirical models.
 - [57] D. M. Heyes, *The Liquid State: Applications of Molecular Simulations* (Wiley, Chichester, UK, 1998).
 - [58] C. N. Likos, A. Lang, M. Watzlawek, and H. Löwen, *Phys. Rev. E* **63**, 031206 (2001).

- [59] C. N. Likos, B. M. Mladek, A. J. Moreno, D. Gottwald, and G. Kahl, [Comput. Phys. Commun.](#) **179**, 71 (2008).
- [60] H. Fragner, [Phys. Rev. E](#) **75**, 061402 (2007).
- [61] B. M. Mladek, Ph.D. thesis, University of Vienna, Vienna, 2007.
- [62] T. Neuhaus and C. N. Likos, [J. Phys.: Condens. Matter](#) **23**, 234112 (2011).
- [63] H. Iglev, M. Schmeisser, K. Simeonidis, A. Thaller, and A. Laubereau, [Nature](#) **439**, 183 (2006).
- [64] B. M. Mladek, D. Gottwald, G. Kahl, M. Neumann, and C. N. Likos, [Phys. Rev. Lett.](#) **96**, 045701 (2006).
- [65] A. A. Louis, P. G. Bolhuis, and J. P. Hansen, [Phys. Rev. E](#) **62**, 7961 (2000).